



Contents lists available at ScienceDirect

Nuclear Instruments and Methods in Physics Research A

journal homepage: www.elsevier.com/locate/nima

The design and performance of a prototype water Cherenkov optical time-projection chamber



Eric Oberla*, Henry J. Frisch

Enrico Fermi Institute, University of Chicago, 5640 S. Ellis Avenue, Chicago, IL 60637, United States

ARTICLE INFO

Article history:

Received 4 September 2015

Received in revised form

21 December 2015

Accepted 12 January 2016

Available online 20 January 2016

Keywords:

Time-of-flight

Cherenkov light

Optical time projection chamber

Microchannel plate photomultiplier

Track reconstruction

Particle detector

ABSTRACT

A first experimental test of tracking relativistic charged particles by 'drifting' Cherenkov photons in a water-based optical time-projection chamber (OTPC) has been performed at the Fermilab Test Beam Facility. The prototype OTPC detector consists of a 77 cm long, 28 cm diameter, 40 kg cylindrical water mass instrumented with a combination of commercial $5.1 \times 5.1 \text{ cm}^2$ micro-channel plate photomultipliers (MCP-PMT) and $6.7 \times 6.7 \text{ cm}^2$ mirrors. Five MCP-PMTs are installed in two columns along the OTPC cylinder in a small-angle stereo configuration. A mirror is mounted opposite each MCP-PMT on the inner surface of the detector cylinder, effectively increasing the photo-detection efficiency and providing a time-resolved image of the Cherenkov light on the opposing wall. Each MCP-PMT is coupled to an anode readout consisting of thirty 50Ω microstrips. A 180-channel data acquisition system digitizes the MCP-PMT signals on one end of the microstrips using the PSEC4 waveform sampling-and-digitizing chip operating at a sampling rate of 10.24 Gigasamples-per-second. The single-ended microstrip readout determines the time and position of a photon arrival at the face of the MCP-PMT by recording both the direct signal and the pulse reflected from the unterminated far end of the strip. The detector was installed on the Fermilab MCenter secondary beam-line behind a steel absorber where the primary flux is multi-GeV muons. Approximately 80 Cherenkov photons are detected for a through-going muon track in a total event duration of ~ 2 ns. By measuring the time-of-arrival and the position of individual photons at the surface of the detector to ≤ 100 ps and a few mm, respectively, we have measured a spatial resolution of ~ 15 mm for each MCP-PMT track segment, and, from linear fits over the entire track length of ~ 40 cm, an angular resolution on the track direction of ~ 60 mrad.

© 2016 Elsevier B.V. All rights reserved.

1. Introduction

We report the design, construction, and performance of a small prototype 'optical time projection chamber' (OTPC) consisting of 40 kg of water viewed by five micro-channel plate photomultipliers (MCP-PMTs). The principle of the OTPC is that with photodetectors with adequate time and space resolution, measuring the time and position of arrival of each individual photon emitted by Cherenkov radiation [1] from charged particles traversing a volume allows the measurement of the photon drift times. Given the arrival positions and the drift times, the track position and direction can be reconstructed, in analogy with reconstructing tracks from the electron drift times in a conventional gaseous or noble liquid TPC.

Due to the faster drift velocity in a medium of photons compared to that of electrons, the expected spatial resolution

measured by timing will be poorer. However, the scale for the required spatial resolution for a large water neutrino detector, for example, is set by the radiation length in water, which is approximately 40 cm [2]. A resolution of less than a few cm per optical sensor may then be adequate to do event tracking for isolated or separated tracks.

The OTPC rests on three enabling technologies:

1. The use of MCP-based photodetectors with a single photoelectron transit-time resolution measured in tens of picoseconds and a correlated position measurement with a resolution measured in mm [3–6], able to cover a large surface area economically. In a conventional large water Cherenkov detector the size of the PMT precludes knowing the position of arrival to within the size of the cathode.
2. The use of microstrip anodes [7,8], with bandwidths matched to the photodetector pulse, to cover large areas while preserving the temporal and spatial information encoded by the incident photon. The microstrips provide spatial resolution along the

* Corresponding author.

E-mail address: ejo@uchicago.edu (E. Oberla).

strip direction from the difference in pulse arrival times at the two ends, and in the transverse direction by charge sharing among strips, allowing mm resolution in two dimensions while requiring only a one-dimensional array of electronics readout channels [9].

3. The development of an economical (in quantity) low-power waveform sampling application specific integrated circuit (ASIC) capable of multiple samples on the rising edge of the fast pulse from an MCP-PMT [4,6], and intrinsic intra-chip jitter measured in picoseconds. In this case we have developed the PSEC4 ASIC, operated at 10.24 Gigasamples-per-second, with an effective dynamic range of 10.5 bits [10].

The OTPC prototype whose design and performance is described below differs from a future large detector in a number of ways. In particular, the small optical path length to the photodetectors allows ignoring dispersion of the photon velocities and scattering in the water, effects that can severely complicate exploiting precise timing for track reconstruction. While a full discussion is beyond the scope of the present paper, there exist strategies to ameliorate the effects: (a) placement of the photodetectors (and potentially mirrors) on the detector surface and inside the volume such that there is always sufficient light with short path-length to seed the initial track hypothesis [11]; (b) restricting the wavelength range to limit the dispersion, making up the resulting inefficiency by additional photocoverage; (c) using statistical methods and the varying of light paths from multiple photodetectors to perform a constrained fit to both the track and the dispersion photon-by-photon [12–14]; and (d) if and when panels of economical large-area LAPPD™ [15,16] photodetectors become available, brute force photocathode coverage on the surface and throughout the volume of the detector, for example.

1.1. A prototype OTPC

To demonstrate this technique, we have built a 40 kg water Cherenkov detector using a combination of commercial MCP-PMTs and optical mirrors. A concept drawing of the optical setup of one of the five MCP-PMT's of this detector is shown in Fig. 1. For each planar MCP-PMT mounted on the water volume, a mirror is mounted on the opposing side creating an image of the Cherenkov light hitting the opposing wall. For a given charged particle track, the mirror adds a discrete set of reflected photons that can be time-resolved from the direct photons, thus economically increasing the photo-detection efficiency over the angular acceptance of the detector.

As the LAPPD MCP-PMTs are not yet available for use outside of a test setup [9,17], this prototype relies on commercial MCP-PMTs that exhibit approximately the same detection resolutions, but with 1/16 the photo-active area per unit. The commercial photodetector used is the Planacon XP85022 MCP-PMT device from PHOTONIS [18]. The total photo-cathode coverage in the prototype OTPC is 125 cm² of the surface area of 1700 cm² that encloses the fiducial volume.

1.2. Organization of the paper

The OTPC prototype detector is described in Section 2, including the design of the optics in Section 2.1 and details on the photodetector modules (PM) in Section 3. The readout system, consisting of the fast waveform sampling digitizers of the front-end and the data-acquisition system (DAQ), is described in Section 4. Section 5 describes the experimental setup in the Fermilab MCenter Test Beam area. The reduction of the raw data to times and positions is presented in Section 6. Section 7 describes the response of the detector to single photons. The OTPC photo-detection efficiency and gain are discussed in Sections 8.1 and 8.2. The test-beam results are shown in

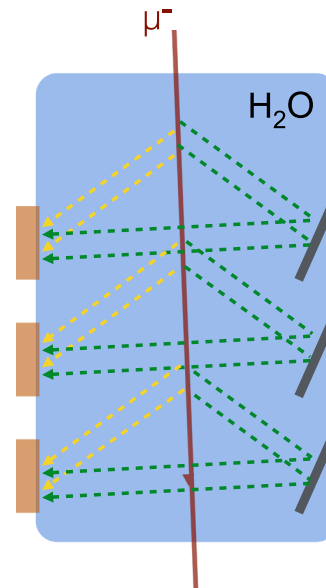


Fig. 1. The concept of the prototype water-based OTPC. A charged particle emits Cherenkov light in the water volume. For each time and spatial-resolving MCP-PMT (left), a mirror is mounted on the opposing side. The mirror adds a discrete set of reflected photons (green) that arrive at the MCP-PMT after a delay due to the extra path length, and can be time-resolved from the direct photons (yellow). (For interpretation of the references to color in this figure caption, the reader is referred to the web version of this paper.)

the final four sections, including the number of photo-electrons along the track (Section 9), resolving the direct and mirror-reflected Cherenkov photons and the time-projection along the beam axis (Section 10), the angular resolution (Section 11), and the spatial resolution of the reconstructed tracks (Section 12). The conclusions are given in Section 13.

2. Detector

The prototype OTPC detector is constructed from a 24 cm inner-diameter poly-vinyl chloride (PVC) cylindrical pipe cut to a length of 77 cm. Six 11 cm diameter ports were machined in the tube arranged in 2 columns of three ports each along the cylindrical axis, as shown in Fig. 2. These columns have an azimuthal separation of 65°. The photodetector modules (PMs), described in Section 3, are mounted on five of these ports (the 6th port was occupied by a conventional PMT used as a diagnostic trigger). The column with 3 PMs installed is denoted the 'normal' view and the other the 'stereo' view.

For each PM, a first-surface broadband optical mirror is mounted on the opposing wall facing the PM port. The 7.6 cm square mirrors are installed on the interior wall of the cylinder at an angle of 24°, denoted as θ_{mirror} in Fig. 3. The remaining exposed PVC surfaces of the interior wall are coated with light absorbing paint [19].

The detector is filled with 40 L of deionized water for the target volume. Because of the detector angular acceptance, the Cherenkov light directionality, and since only the first five ports are instrumented, the effective fiducial volume is limited to roughly the top two-thirds of the total volume, corresponding to a fiducial mass of ~ 25 kg.

2.1. Detector optics

The optical properties of the detector components in the light path, as quoted by the manufacturers [18,19], are shown vs. wavelength

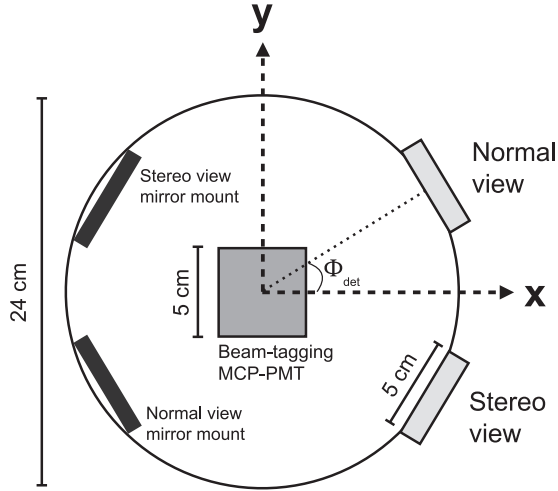


Fig. 2. Rear-view scale drawing of OTPC detector showing the normal and stereo MCP-PMT mounting positions. The normal and stereo mounted PMs are symmetrical about the x-axis in the OTPC coordinate system, and separated by an azimuthal angle of $\phi_{det} = 32.5^\circ$. The beam comes out of the page in the +z direction.

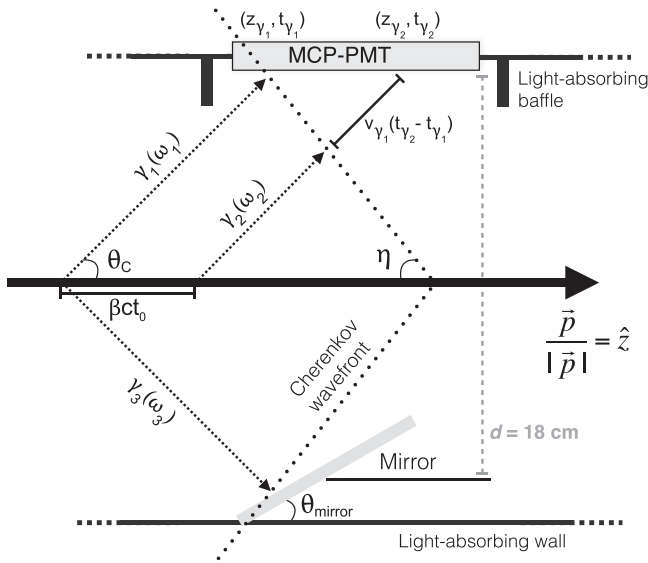


Fig. 3. Two-dimensional projection of the Cherenkov light generated by a relativistic charged particle (heavy, black arrow) and the OTPC optics. The drawing shows the optical paths of three photons: γ_1 and γ_2 are directly detected, γ_3 is reflected at the mirror. The mirror is mounted at an angle, θ_{mirror} , of 24° .

in Fig. 4. Despite efforts to capture as much near-UV Cherenkov light as possible by using fused-silica windows, we found that these wavelengths are cut off by the optical coupling gel between the window of the port and the MCP-PMT. The characteristics of the light-absorbing paint were modeled with a broadband 95% absorbance and a 5% diffuse reflectance. A full detector simulation was built using the Chroma toolkit [20].

With MCP-PMT photodetectors having time resolutions of 100 ps or less and high spatial granularity, the water chromaticity and scattering properties become important as the distance from the particle track to the photo-detector increases. The Cherenkov photons, which are generated at an angle specified by the phase velocity of the dielectric medium, propagate at the group velocity, the speed at which energy is transported in the dielectric, given by [21]:

$$v_g(\omega) = \frac{c}{n_g(\omega)} = \frac{c}{n(\omega) + \omega(dn/d\omega)} \quad (1)$$

where $n(\omega)$ and $n_g(\omega)$ are the phase and group index of the medium,

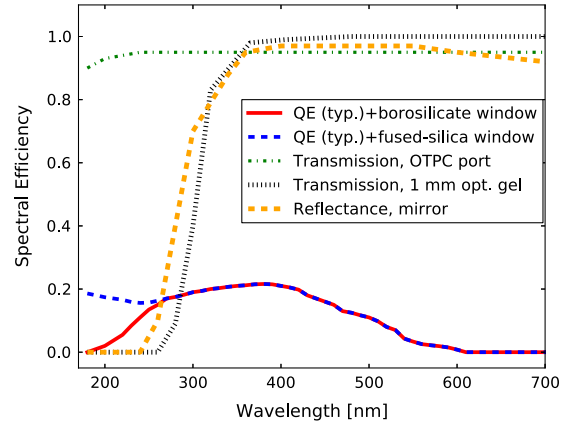


Fig. 4. Optical properties of the OTPC optical components over wavelength range of 200–700 nm. These parameterizations are used to model the optical properties in a simulation of the detector using the Chroma toolkit [20].

respectively. The group index is both greater in magnitude and more dispersive than $n(\omega)$ as shown in Fig. 5(a).

The spectrum of detected photons is the convolution of the OTPC spectral response and the Cherenkov spectrum [22]. A simulation of 10^4 muons with a uniform distribution of energies between 1 and 10 GeV gives a spectrum of detected photons of 370_{-50}^{+110} nm, with the spread covering about 95% of the spectrum around the mean wavelength. Over this wavelength range, $\langle n/n_g \rangle \approx 0.97$.

The relative timing errors due to chromatic dispersion of the group velocity are shown in Fig. 5(b). At the maximum photon drift-length in the prototype OTPC (≈ 30 cm), the expected timing error is about ± 25 ps, which is small compared to the 75 ps single-photon timing resolution of the OTPC system shown in Section 7. Averaging over the dispersion effects, the effective photon drift-speed in the OTPC is given by the weighted average of the group velocity over the detected photon spectrum, $\langle v_{group} \rangle = 218 \text{ mm ns}^{-1}$.

Chromatic errors on the Cherenkov angle are also considered. For particles with $\beta = 1$, $\theta_c = 0.743_{-0.007}^{+0.008}$ rad over 95% of the detected photon spectrum. For the longest photon path lengths of ~ 30 cm, this introduces maximum spatial (time) errors of 2.4 mm (~ 10 ps), which are comparable or smaller than the photon detection resolutions in the prototype OTPC. The direct (non-reflected) photons travel less than 15 cm, correspondingly reducing dispersion effects.

2.2. Track reconstruction equations

In the limit of negligible dispersion of the Cherenkov light, an analytic approach can be taken to reconstruct particle tracks. Consider a particle traveling through the OTPC as shown in Fig. 3, but further generalizing the track by allowing a polar angle, θ_i , with respect to the z-axis (see the caption of Fig. 2). Two Cherenkov photons generated along the particle path at $t=0$ and $t=t_0$ are detected with a relative time and longitudinal position of $\Delta t_{\gamma_{21}} = t_{\gamma_2} - t_{\gamma_1}$ and $\Delta z_{\gamma_{21}} = z_{\gamma_2} - z_{\gamma_1}$. The relative timing of the direct photons is given by

$$\Delta t_{\gamma_{21}} = t_0 + \left(\frac{L_{\gamma_2}}{v_{\gamma_2}} - \frac{L_{\gamma_1}}{v_{\gamma_1}} \right) = t_0 + \frac{\Delta L_{\gamma_{21}}}{\langle v_{group} \rangle} \quad (2)$$

where $\Delta L_{\gamma_{21}}$ is the path length difference and $\langle v_{group} \rangle$ is the weighted average of the group velocity over the optical range of the detector. The experimentally measured relative times and

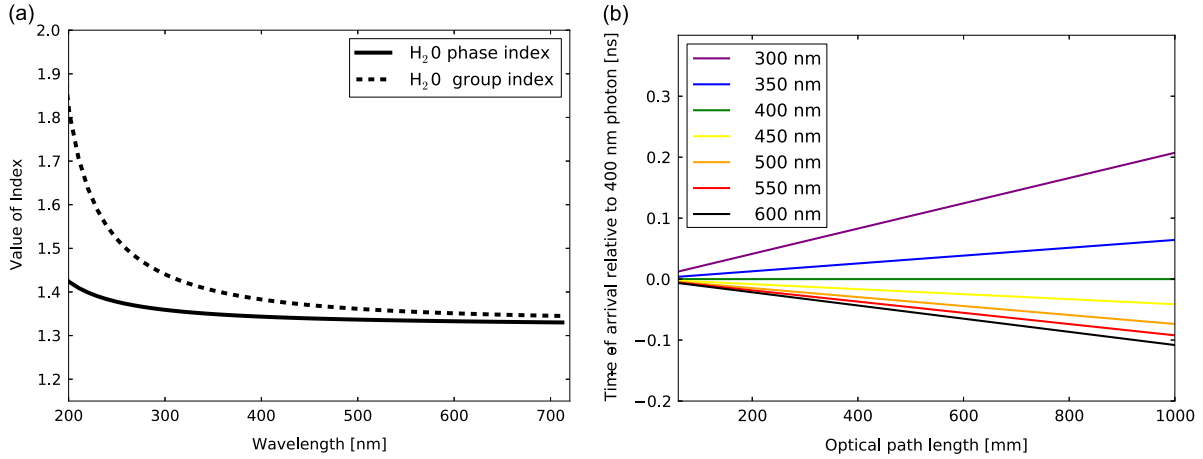


Fig. 5. (a) Phase and group indices of refraction in water over the optical wavelength range. The water phase-index of refraction data were taken from [23]. (b) Timing errors due to chromatic dispersion of the group velocity, referenced to a 400 nm photon, vs. optical path length.

z-positions in terms of the track variables are

$$\Delta t_{\gamma_{21}} = t_o \left(1 - \frac{\beta c}{\langle v_{group} \rangle} \tan \theta_i \right) \quad (3a)$$

$$\Delta z_{\gamma_{21}} = \beta c t_o \cos \theta_i. \quad (3b)$$

A useful relation is the time-projection on the z coordinates. The projection over an infinitesimal track length is

$$\frac{dt}{dz} \approx \frac{1}{\beta c} \frac{\tan \theta_i}{\langle v_{group} \rangle} \quad (4)$$

for small angles along a path parallel to the detector plane. The OTPC photon drift speed in Eq. (4) is given by $\langle v_{group} \rangle$.

An additional set of reflected photons is detected at each MCP-PMT from a mirror mounted on the opposite side of the inner cylinder as shown by γ_3 in Fig. 3. This is not a necessary ingredient of an OTPC, but is an effective and economical method of increasing limited photocathode coverage. Each mirror is mounted at an angle θ_{mirror} of $(90^\circ - \theta_c)/2 \approx 24^\circ$. For a small range of particle angles, the mirror creates a time-delayed image of the Cherenkov light on the opposing wall at the MCP-PMT.

The discrete mirror positions provide a technique to measure the longitudinal track location across a single PM by using the measured time difference between the direct and mirror-reflected Cherenkov light. For particle trajectories with small angles along the OTPC axis, the time-difference between a direct and mirror-reflected photon measured at the same z-position on the MCP-PMT is

$$\Delta t(z) = \frac{1}{\langle v_{group} \rangle} \left(\frac{2r}{\sin \theta_c} + d(z) \right) - \frac{1}{\beta c} \left(\frac{2r}{\tan \theta_c} \right) \quad (5)$$

where r is the track displacement from the OTPC center-line and $d(z)$ is the inner cylinder diameter along the z-axis between the angled mirror and the MCP-PMT photocathode. The first term in Eq. (5) is the time separation from the path-length difference between the direct and mirror-reflected photons, whereas the second term accounts for the time-difference at which the photons were emitted along the particle track in order to arrive at the same z-position at the PM. Averaging over the dispersion effects and using $\beta=1$, we insert values in Eq. (5) and solve for the track displacement:

$$r = 0.737(\Delta t(z)\langle v_{group} \rangle - d(z)). \quad (6)$$

The scaling factor accounts for relative optical path lengths when the particle is off the OTPC center-line. The mean value of $d(z)$ is 18 cm, which is the distance from the angled mirror center-point to the photo-detector module as shown in Fig. 3.

3. Photodetector module

The OTPC is instrumented with five photodetector modules (PM), which provide the photon detection using the commercial ‘Planacon’ XP85022 MCP-PMT device from PHOTONIS [18]. These square devices have a $5 \times 5 \text{ cm}^2$ photo-active area and an anode comprised of a 32×32 square pad array with a 1.6 mm pad pitch. The three MCP-PMTs mounted in the normal view are 25 μm MCP-pore-size tubes with fused silica windows manufactured in 2014–2015. On the stereo view are 2 MCP-PMTs; one from the same manufacturing run, and another considerably older MCP-PMT with a borosilicate window. The latter MCP-PMT exhibited lower gain and detection efficiency.

While reading out each of the Planacon’s 1024 anodes might provide the best-case granularity and pile-up rejection per channel, it presents a challenge when instrumenting a detector with many such photo-detectors. Instead, we adopt a similar microstrip readout scheme as the first-generation glass package LAPPDs [8,7]. A 32 channel microstrip anode PCB board was designed such that a column of 32 anode pads is mapped to a single 50 Ω transmission line. Each microstrip line serves as both the DC return and the high fidelity signal path for $\frac{1}{32}$ of the MCP-PMT. The central 30 strips are digitized while the two edge strips are terminated at 50 Ω . The board-mounted photo-tube is shown in Fig. 6.

The accelerated electron shower from the MCP will induce an electromagnetic wave between the microstrip’s signal and reference plane, which will propagate equally along both directions on the 1D microstrip. We use a pair of high-density multi-channel 50 Ω coaxial cables to bring these waveforms off the board [24]. The readout strategy adopted for the OTPC is to digitize the waveforms on the microstrips at only one end, leaving the multi-channel cables at the other end unterminated. Thus, the wave that initially propagates along a transmission-line microstrip towards the open end will be reflected with the same polarity back towards the digitizer for that strip, which then captures the waveforms caused by the initial pulse in both its direct and reflected manifestations (see Fig. 6 and Section 4).

For a single photo-electron signal, the digitizer will record two transient waveforms along the microstrip. The times of the direct and open-end reflected waves, t_1 and t_2 can be extracted from these transients, as diagrammed in Fig. 6. Using the measured times we can solve for the photon longitudinal position, x , and time-of-arrival, t_o :

$$x = v_{prop} \frac{t_2 - t_1}{2} - \frac{D + 2C_1}{2} \quad (7a)$$

$$t_0 = \frac{t_2 + t_1}{2} - \frac{1}{v_{prop}}(D + C_2 + C_1) \quad (7b)$$

where D , C_1 , and C_2 are the microstrip lengths of the MCP-PMT footprint, the reflected wave cable length, and the direct wave cable length, respectively. The wave speed along the microstrip is v_{prop} , and is derived in Section 7.1. A ‘10’ (25.4 cm) high density coaxial cable provides a delay for the reflected signal and an identical ‘6’ (15.2 cm) cable connects the microstrip card to the waveform digitizer board [24].

4. Front-end data acquisition

The waveforms on the anode microstrip of each PM are digitized at 10.24 Gigasamples-per-second (GSPS) using the ‘Acquisition and Digitization with psec4’ (ACDC) printed circuit card. This card uses 30 channels of the PSEC4 ASIC with an analog bandwidth ≥ 1 GHz [10]. The signal input to the PSEC4 is AC-coupled and the on-chip signal voltage range is from 0.1 to 1.1 V. A pedestal

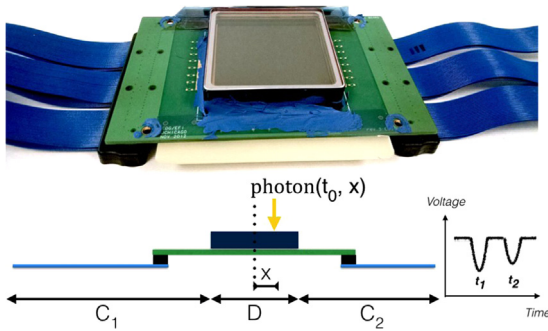


Fig. 6. A PHOTONIS XP85022 Planacon MCP-PMT [18] mounted on a custom 32 channel, 50Ω transmission line anode board is shown in the top photograph. The Planacon has an anode of 1024 pads in a 32×32 array over the $5 \times 5 \text{ cm}^2$ active area. These are mapped to the microstrip anode readout card in rows of 32. The bottom diagram outlines the technique for using the single-channel waveform timing to extract the incident photon position along the transmission line. The times of the direct and open-end reflected waves on the anode microstrip are denoted by t_1 and t_2 .

voltage-level of 0.8 V is set for the OTPC data runs, allowing ample headroom for negative polarity pulses. The digitized waveforms from the PSEC4 chips are sent to an on-board field-programmable gate array (FPGA), which buffers the digital data. Serial communication and data readout to a system data acquisition card are performed over a low-voltage differential signaling (LVDS) cable link.

The ACDC card runs off a 40 MHz clock that is up-converted within the PSEC4 ASIC using a voltage-controlled delay line (VCDL) to achieve a 10.24 Gsa/s sampling rate over 256 sample cells [10]. Though an effective and power-efficient means of garnering high sampling rates, the VCDL-controlled switch capacitor array has non-uniform time-steps due to process variations in the integrated circuit fabrication ($\sim 10\%$) spread in time-steps in PSEC4 [10]. Methods of calibrating of the time-base of PSEC4 and related CMOS chips are discussed in [10,25,26]. A complete, end-to-end PSEC4 time-base calibration was not performed on the data presented here, instead a first-order correction is applied such that the integral non-linearity over the time-base is zeroed. With this crude correction, a nominal time-step of 97 ps per PSEC4 sample is assigned.

5. Experimental setup

The OTPC was installed on the beam line of the MCenter secondary beam at the Fermilab National Laboratory Test-Beam Facility [27], approximately 3 m behind a 1.09 m thick steel absorber. The absorber served as both a beam-stop for the secondary beam so that the dominant particle type seen by the OTPC was muons, and as a target station and collimator to generate a tertiary beam utilized by the LARIAT experiment, to which we operated parasitically [28].

A side view of the installed OTPC is shown in Fig. 7 where the upstream absorber is out of the frame. The five OTPC PM modules are mounted facing inwards on the water volume. Each of the PMs is connected to the system central cards over two Category 6 (CAT6) network cables. The system cards interface to a remotely controlled Linux PC on an adjacent rack that also houses the beam trigger coincidence and discrimination logic. High voltage (HV) is supplied to the detector from the counting room over ~ 200 m

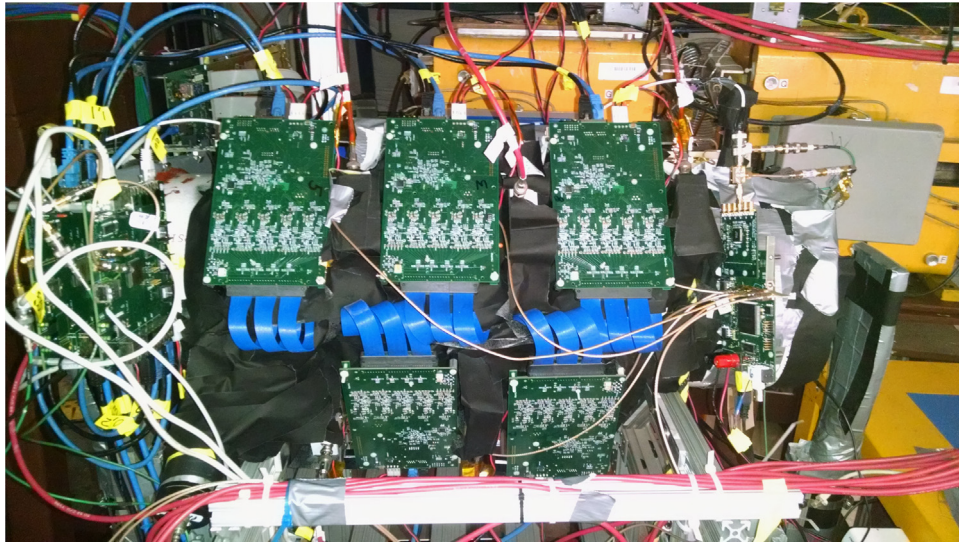


Fig. 7. The prototype OTPC installed in the MCenter enclosure hall at the beam height of 208 cm. The upstream steel absorber block is out of the frame to the right. Mounted facing inwards, the five PMs connect to the system data acquisition (DAQ) cards that are mounted on the left. The DAQ system connects to a remotely controlled laptop on an adjacent rack, which also houses the beam trigger coincidence and discrimination logic. The yellow dipole magnets on the adjacent tertiary beam-line used by the LARIAT experiment are visible in the background. (For interpretation of the references to color in this figure caption, the reader is referred to the web version of this paper.)

SHV cables; the low voltage for the electronics is supplied within the enclosure. The OTPC water volume corresponds to 2.1 radiation lengths along the cylindrical axis.

The beam was delivered to the Meson Lab during the 4.2-s slow-spill at the beginning of the 60 s Fermilab accelerator complex ‘super cycle’. During the OTPC test-beam runs, a secondary beam of positive pions impinged on the MCenter target at momenta of 8, 16, or 32 GeV/c. Because the OTPC was located behind the secondary beam absorber, the particle flux was dominated by muons (85%), with a mixture of hadrons (10%), electrons (1%), and photons (4%) from punch-through and showering, as verified in a G4beamline simulation at a beam momentum of 16 GeV/c [29].

5.1. The beam trigger

The beam trigger consists of a pair of external scintillator detectors and a pair of Cherenkov detectors as shown in Fig. 8. The pair of $5 \times 5 \text{ in}^2$ plastic scintillators mounted fore (S_1) and aft (S_2) of the OTPC provide good coverage over the OTPC cross-sectional area.

The two Cherenkov detectors, R_1 and R_2 , consist of MCP-PMTs with fused-silica Cherenkov radiators on their front faces that provide a prompt beam-trigger signal as the beam particle traverses the radiator and MCP-PMT. R_1 , mounted on the front cap of the OTPC, consists of a PHOTONIS XP85011 MCP-PMT with an anode structure consisting of an 8-by-8 array of pixels, viewing a small cylindrical (1 cm diameter) fused-silica radiator mounted in its center. The R_1 signal is made by summing the central 32 pixels through 10Ω series resistors on each pixel, forming a single pixel of $1 \times 1 \text{ in}^2$ active area. The second Cherenkov counter, R_2 , is mounted on the rear of the detector (see Fig. 2), and consists of a PHOTONIS XP85022 MCP-PMT with an anode structure of 32-by-32 pixels read out by a 30-microstrip anode board, coupled to a matching 5 mm thick square fused-silica radiator.

Twenty-nine of the 30 R_2 strips are read out and digitized with an ACDC board in the same manner as the PMs, allowing spatial and time-tagging of the out-going particle. The signal from R_1 is recorded in the 30th channel, which allows for a time-of-flight measurement for each through-going particle with approximately 100 ps resolution.

The beam trigger signal is made with standard NIM electronics. The signals S_1 , S_2 , and R_1 are discriminated and fed to a coincidence unit. Two configurations were used during data runs: (1) $S_1 + S_2 + R_1$ and (2) $S_1 + R_1$. Trigger configuration (1) is the default through-going particle trigger. Configuration (2) allowed the recording of particles that may scatter out, stop, or shower within the water volume. Both digital trigger signals are sent to the OTPC data acquisition system, which then passes these trigger signals to the front-end ACDC cards. For further details on the trigger system see [30].

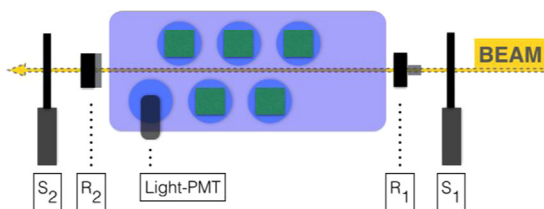


Fig. 8. Diagram of the external beam-trigger (not to scale). The beam trigger coincidence can be made between four sub-detectors: the front and back scintillators+PMTs (S_1 and S_2), and the front and back fused-silica Cherenkov radiators+MCP-PMTs (R_1 and R_2). An additional diagnostic trigger is generated by a ‘1’ PMT (‘Light-PMT’) mounted on the last OTPC port to observe Cherenkov light in the water volume.

6. Data reduction

An OTPC event is recorded using 180 channels of 10.24 GSPP data in a time window of 25 ns. The first 150 channels contain the data from the OTPC photodetector modules (PM) and the remaining 30 channels, 150–178, contain the trigger information from the R_2 detectors (described in Section 5.1). The digitized signal from R_1 (see Fig. 8) is saved in channel 179 and is used as a coarse zero-time reference.

The following procedures are performed on these data before analyzing an event:

1. A pedestal calibration is performed for each of the 256 sample cells in all PSEC4 channels [10].
2. The firmware time-stamps are checked on the front-end ACDC boards. If the time-stamps are not synchronized, the event is discarded.
3. The Cherenkov data on all channels are located in the PSEC4 buffer using R_1 peak-signal time.
4. A reference baseline level, created using the median value of the 50 samples preceding the pulses, is subtracted from each channel.
5. A time-base is constructed from the PSEC4 samples after applying the time-base calibrations. The data points are cubic-spline interpolated to have an evenly spaced event time-base of 97 ps per sample.

At this point in the data reduction process, the event is aligned with respect to the R_1 trigger signal, baseline-subtracted, and referenced to a time-base. The event size is: 180 channels \times 12 bit ADC counts \times 260 time-steps over 25 ns (70 kB).

The event is further reduced by extracting the trigger information in channels 150–179, narrowing the event time-window to hold only the region of Cherenkov photon hits, and removing below-threshold channels as shown in Fig. 9 [30]. After the data reduction, the event comprises the following trigger information: particle output x -position, particle output y -position, time-of-flight, R_1 trigger time, R_2 trigger time, R_1 total charge, R_2 total charge, and the number of distinct hits in R_2 . The reduced size of the event time-stream data is: number of OTPC channels above threshold (≤ 150) \times 12 bit ADC counts \times 110 time-steps over 10.67 ns (number of channels \times 0.17 kB).

6.1. Extracting the photon time-of-arrival

For each detected photon, we measure its 2D spatial position on the OTPC cylinder (z_{det} , ϕ_{det}) and its time-of-arrival, t_{det} . By projecting the measured photon arrival times on the two spatial coordinates we can reconstruct the charged particle track in 3D. We take the detected photon azimuth angle, ϕ_{det} , to be the PM location about the OTPC cylinder and its z -position, z_{det} , as the microstrip position along the OTPC longitudinal axis. There are 2 discrete ϕ_{det} angles and 150 discrete z_{det} positions. This section describes how we extract the time-of-arrival for each photon from the digitized waveforms.

We found that a robust algorithm is to interpolate the PSEC4 waveform in a small region around the peak. A window of 4 time-steps (97 ps each) is interpolated with a cubic spline on a 9.7 ps grid and the pulse time is taken from the peak of the interpolated region. An example of an OTPC channel hit by a Cherenkov photon is shown in Fig. 10.

For an event, the output of the peak-interpolation algorithm is a set of times ($[t_{1a}, \dots], [t_{2a}, \dots]$) from the direct and anode-reflected pulses. To get the photon hit time, we apply Eq. (7b) and require causality using Eq. (7a). That is, the time difference between the direct and anode-reflected pulse should be located on the

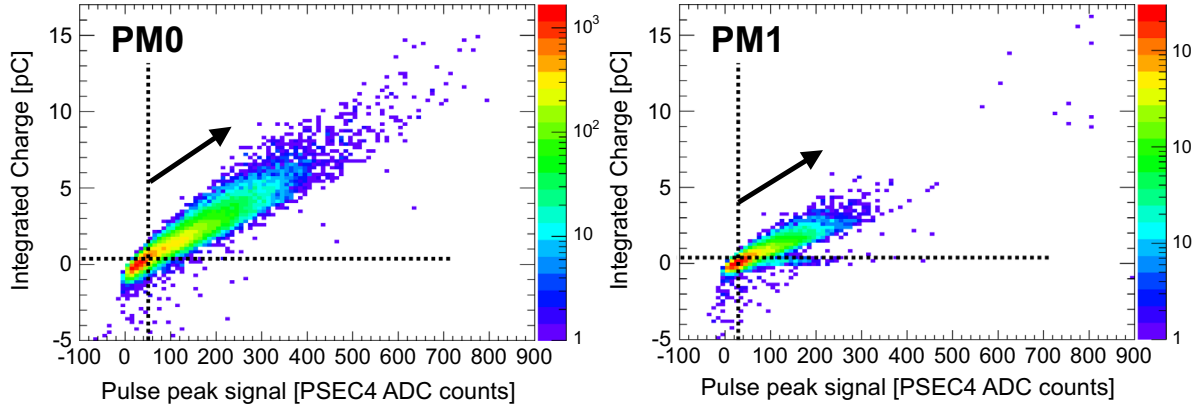


Fig. 9. Correlation plots of integrated charge vs. pulse peak signal for PMs 0 and 1. Channels with waveforms above a minimum integrated charge and ADC count threshold, shown as dashed lines, are saved and further processed to measure the photon time-of-arrival.

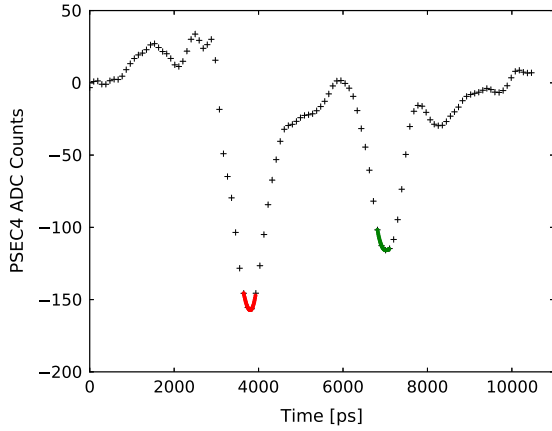


Fig. 10. OTPC digitized waveform from a Cherenkov photon. A single photo-electron waveform is shown with the peak-interpolation time-extraction method. The interpolated peak-signal regions on the waveform are shown in red (green), which represent the direct (anode-reflected) pulses. (For interpretation of the references to color in this figure caption, the reader is referred to the web version of this paper.)

microstrip line within the 5 cm length of the MCP-PMT. The causality requirement is that $t_{2a} - t_{1a} \in [3.1, 3.9]$ ns after solving Eq. (7a) for the cable lengths in the PM.

7. Single photo-electron response

A laser test-stand was built to characterize the single photo-electron response of the PMs. A 405 nm PiLas laser was used in pulsed mode, which can achieve pulse widths of 33 ps FWHM [31].

7.1. Single-photon

The single photo-electron position resolution is obtained by scanning the laser beam, attenuated to the single-photon level, on the active area of the PMs both parallel and transverse to the microstrip direction. Results from a scan along the microstrip direction are shown in Fig. 11. Four data points were taken at a spatial separation of 4.5 mm with a time-difference resolution of ~ 35 ps measured for all laser positions. This is the inherent electronics timing resolution for the single photo-electron pulses digitized using one channel of the PSEC4 chip, with the basic (not complete) time-base calibration described in Section 4.

Fig. 11 shows the time difference along the microstrip vs. the laser beam position, from which the signal propagation velocity,

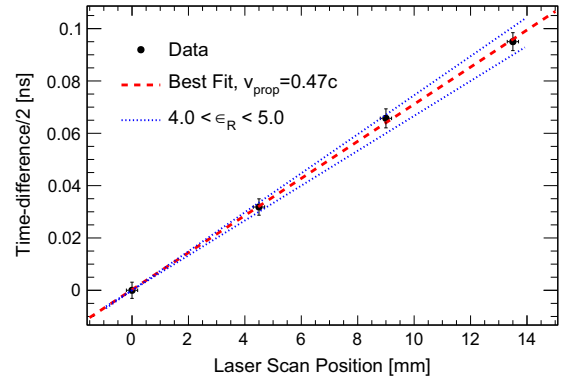


Fig. 11. Single photo-electron laser scan to measure the propagation velocity along the microstrip line. The vertical error bars are the 3σ standard error on the time-difference measurement (the single event statistical error on the time-difference is ≤ 35 ps for all laser positions). The data agree with the expected velocity given the typical dielectric permittivity of an FR4 printed-circuit board substrate ($\epsilon = 4.3 \pm 0.2$).

v_{prop} , in Eq. (7) along the microstrip to be calculated. The best fit v_{prop} is found to be $0.47 \pm 0.02c$.

7.2. Multi-photon

A similar test is employed to measure the relative timing between single photons within the same laser pulse. In this setting, an iris is aligned with the laser beam axis and a 10 mm focal length convex lens is put in the laser path. The MCP-PMT sits 30 cm behind the lens, which projects an elliptical laser beam spot over the MCP-PMT active area. A neutral density filter is installed after the lens to attenuate to an average of a few photons per pulse.

Events are analyzed that have two recorded photo-electrons, in which the signals are clearly separated between channels above and below the MCP-PMT center-line. The relative timing between photons is shown in Fig. 12. A tail is seen in the distribution, which is likely caused by optical reflections in the test setup that are recorded late. The core resolution is shown to be 105 ps, which corresponds to a single photo-electron PM resolution of 75 ps.

From these measurements, we conclude that the $1-\sigma$ single photo-electron time-of-arrival and space statistical errors are $(\sigma_t, \sigma_x, \sigma_y) = (75 \text{ ps}, 2 \text{ mm}, 3 \text{ mm})$. The σ_x resolution is taken from the microstrip pitch on the anode board.

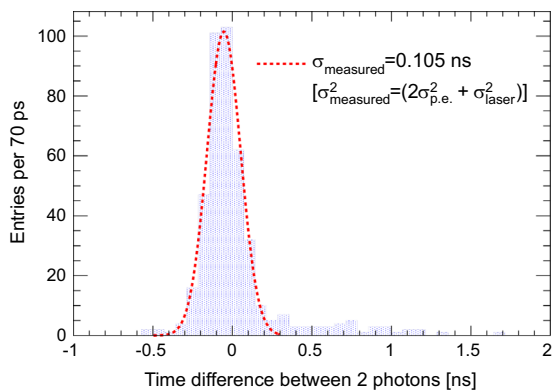


Fig. 12. Relative timing measurement between 2 photons on the PM. The underlying single photo-electron electronics + MCP-PMT timing resolution for this measurement is 75 ps.

8. Photo-detection properties

Photo-detection properties were derived from a dataset of 1686 events taken in 16 GeV/c secondary beam runs using the beam-trigger configuration 1 as described in Section 5.1.

8.1. Photo-detection efficiency

A comparison between data and the expectation from simulation shows a 70–80% detection efficiency compared to our detector Monte Carlo, which assumes optimal coupling and equal photo-response at each PM. We estimate that the losses of the direct Cherenkov light are due to: (1) $10 \pm 5\%$ due to reflection losses (spots poor optical-gel coupling would lead to total-internal reflection) and (2) $6 \pm 3\%$ due to light cut off by a baffle around the photodetectors. Additional light collection inefficiencies (for both direct and reflected light) are: (3) $5 \pm 1\%$ from the lower efficiency of PM1 and (4) $3 \pm 1\%$ from 5 readout channels with poor coupling, which were removed from the analysis chain. These estimates are consistent with the overall observed detection efficiency, and the measurements of the lower number of direct photons relative to reflected photons shown in Section 10.1.

8.2. Single photo-electron gain

The gain per channel is shown in Fig. 13, which is the multiplicative gain of the MCP-PMT, the 20 dB pre-amplifier board, and any relative gains between channels in the PSEC4 ASIC.¹ This is measured by taking the median integrated charge for signals above threshold over the dataset. Error bars are taken to be the RMS of the integrated charge distribution per channel. MCP-PMT gains of about 10^6 are found for PMs 0 and 2–4, who are measured to be about twice the gain of PM 1. The gain on each channel is used to calibrate the number of detected photo-electrons per event.

9. Photo-electrons along the track

Four raw time-projected events are shown in Fig. 14. The PSEC4 time-step is plotted vs. the OTPC channel, which is divided into 5

¹ Since a full voltage calibration was not performed on these data, there exist small gain differences between PSEC4 channels due to their relative transfer functions from input voltage to output ADC counts. The vast majority of signals are small ($< 10\%$ of the PSEC4 voltage range [10]), so this is not a large effect.

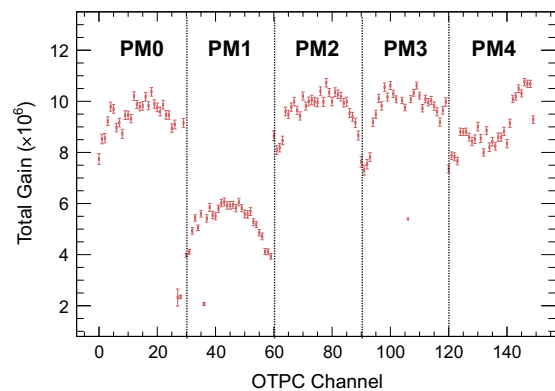


Fig. 13. The OTPC per-channel gain. PMs 0, 2, and 4 constitute the OTPC normal view; PMs 1 and 3 are in the stereo view. The gain factor on each channel is comprised of three factors: the MCP-PMT \times electronics pre-amp gain \times variations in the PSEC4 count-to-voltage transfer function.

sub-panels representing each PM. The raw PSEC4 signal amplitudes are normalized with respect to the average gain on each PM. The beam direction is from left-to-right. The two time-separated pulses for every signal channel are the direct and anode-reflected waveforms. These data are reduced up to step 5 in Section 6.

Events (a) and (b) in Fig. 14 are from the 16 GeV/c data that were recorded using the through-going trigger configuration. Events (c) and (d) are from the 8 GeV/c data, which were recorded using trigger configuration 2. These two tracks left no signal in R_2 , implying that these particles interacted in the volume, or else somehow missed the back trigger detector.

By applying the channel-to-channel gain calibration described in Section 8.2, we can measure the effective number of photo-electrons along the track. Fig. 15 shows the number of detected photons along the OTPC z-axis for the events in Fig. 14. Event (a) has a roughly uniform number of photo-electrons along the ~ 40 cm extent of the photo-detection coverage. Event (b) shows an increase in the detected photons in the last one-third of the track, possibly due to the creation of a δ -ray along the track. Events (c) and (d) are distinct in that they exhibit a large localized peak in the number of detected photons, suggesting that these events may have an EM showering component. Event (c) could also be explained by an wide-angled muon track, either from the beam or an accidental cosmic ray, that exited the OTPC volume at PM 0.

10. The time-projection

In this and the following sections we use 1230 events from a secondary beam momentum of 16 GeV/c dataset, which were triggered on through-going tracks at the best measured water quality.

We now add the time dimension of the detected photons, as extracted from the waveforms in Section 6.1, to the data analysis. Fig. 16 shows the measured time structure of the events, in which the times-of-arrival of the Cherenkov photons on the OTPC normal view are plotted with the measured times of the beam trigger signals, R_1 and R_2 . The time structure seen in the Cherenkov photon data is due to the three discrete PM locations in the OTPC normal view.

10.1. Resolving the direct and mirror-reflected Cherenkov photons

As shown in Eq. (4), the particle's time-projection along the longitudinal axis has two components: one from the particle's velocity and the other from its angle with respect to the OTPC

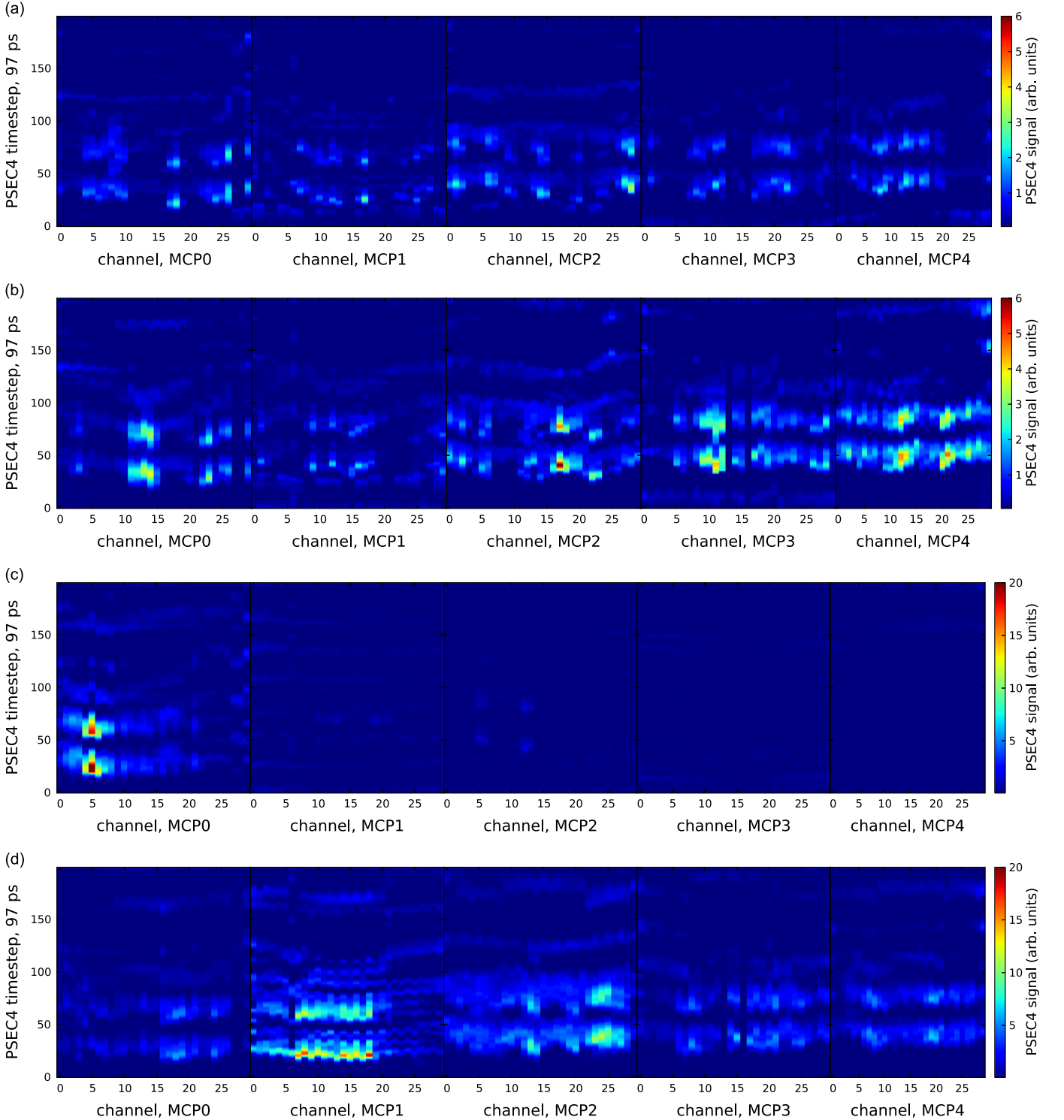


Fig. 14. Raw OTPC events: time-step (97 ps per bin) vs. OTPC channel. The 5 panels in each event are the individual OTPC PMs. PMs 0, 2, and 4 constitute the OTPC normal view, PMs 1 and 3 are in the stereo view. The raw PSEC4 signal amplitudes are normalized with respect to the average gain on each PM. (a) Typical through-going event that is representative of most recorded events. (b) Through-going event, in which the number of detected photons increases near the right side. (c) Track with a large number of photons over a short extent. (d) Large signal amplitude along entire track, peaking in the second panel. Events (c) and (d) were recorded using trigger configuration 2 (Section 5.1). Events (a) and (b) were recorded using configuration 1, the through-going trigger mode.

z -axis. For through-going multi-GeV muons, we can assume the particle's velocity is constant along the OTPC with $\beta=1$. We introduce the position-corrected time, t' , which nulls out the velocity term in Eq. (4):

$$t'_i = t_i - \frac{z_i}{c} \quad (8a)$$

$$\frac{dt'}{dz} = \frac{dt}{dz} - \frac{1}{c} = \frac{\tan \theta}{\langle v_{group} \rangle} \quad (8b)$$

where t_i and z_i are the measured individual photon times and z -positions. As defined in Section 2.1, $\langle v_{group} \rangle$ is the weighted average of the group velocity dispersion over the optical efficiency range of

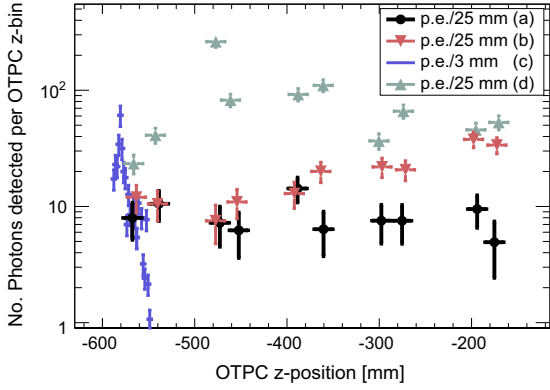


Fig. 15. The number of photons detected along the OTPC z-axis, per z-bin defined by the horizontal error bars, for events presented in Fig. 14. The gain calibrations shown in Section 8.2 were used to convert the waveform integrated charge to a number of photo-electrons (p.e.). Events a, b, and d show the number of p.e.'s per 2.5 cm interval along the OTPC z-axis. Event c shows the number of p.e.'s per 3 mm.

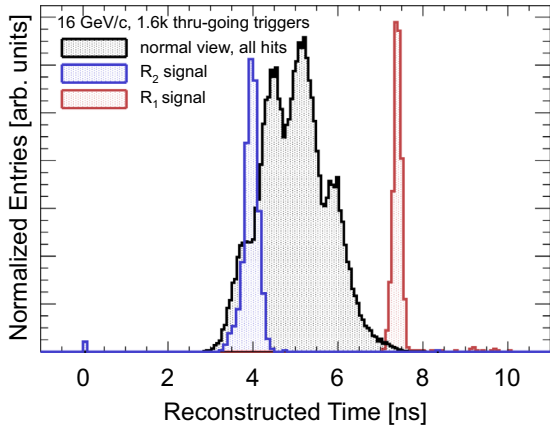


Fig. 16. The times of the data and trigger signals from the reduced 16 GeV/c dataset. The reconstructed times of the detected Cherenkov photons (from the normal-view) are shown by the black histogram. The ‘fast’ trigger signals, R_1 and R_2 are shown in the red and blue, respectively. Each event is aligned with respect to the R_1 time. The time of R_1 is measured later than the R_2 signal due to cable delays. (For interpretation of the references to color in this figure caption, the reader is referred to the web version of this paper.)

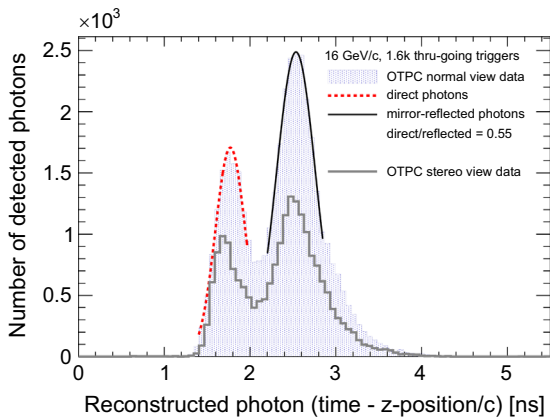


Fig. 17. Histogram of the inclusive dataset of detected photons using the position-corrected time: $t'_i = t_i - z_i/c$. This removes the contribution to the time-projection along the z-axis due to the particle's velocity (assuming $\beta=1$). The direct and mirror-reflected Cherenkov photons are distinctly visible and separated by 770 ps, as taken from the fit parameters.

the detector. In the t' basis, the time-projection along the OTPC z-axis is a measure of the particle angle.

Fig. 17 shows the distribution of the measured photon times in terms of their position-corrected time, t'_i . The R_2 trigger time for each track serves as a fine time-alignment between events. As expected, the t' distribution is bi-modal with peaks corresponding to the direct and mirror-reflected photons. A distinct separation of 770 ps is observed, which is consistent with the path length differences between the direct and reflected photons divided by the photon drift velocity, $\langle v_{group} \rangle$. The path length difference is given by the range of distances between the angled mirror and PM photocathode, 18 ± 1 cm (Section 2.2), which corresponds to an expected time difference between the direct and mirror-reflected photons of 830 ± 50 ps.

Fig. 17 also shows a larger number of mirror-reflected photons than direct photons. Using the relative areas from the Gaussian fits to the distributions, we measure fewer direct than reflected photons by a factor of 0.55 in the normal view data. This was unexpected; the detector Monte Carlo predicts approximately equal numbers of each for small-angle tracks. The relative deficit of direct photons is most likely due to reflections of the direct light at the fused-silica OTPC port and MCP-PMT interface as discussed in Section 8.1. It is also likely that there is a small percentage of scattered photons in the data; these would arrive later than the direct photons and may be included in the mirror-reflected distribution and also cause the observed tail in the t' timing distribution after 3 ns.

10.2. An example event

Fig. 18(a) shows the time-projection on the z-axis for the raw event shown in Fig. 14(a). In this event, 73 individual photons were resolved in both time and space. Fig. 18 shows their measured times, t_i , projected vs. their detected positions, z_i . The photons detected in the normal and stereo views are denoted by black and red data-points, respectively. Fig. 19 is a histogram of the position-corrected times, t'_i , of this event. The peaks in the histogram are from the measured arrival-times of the direct and mirror-reflected photons.

11. Angular resolution

The direct Cherenkov photons can be used to measure the particle angle with respect to the OTPC z-axis as shown in Eq. (8a). The most straightforward method of extracting this angle is to assume a linear track over the extent of the OTPC photodetector

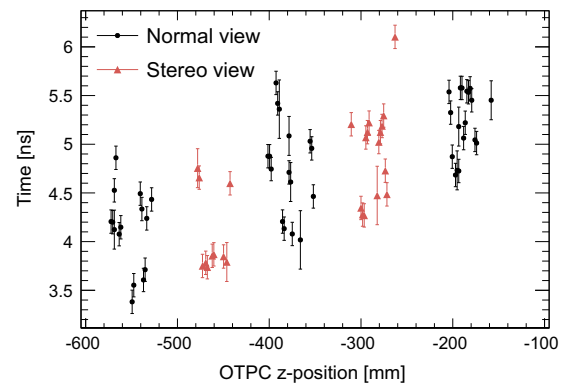


Fig. 18. The time-projection along the beam axis for a single event. The time projection along the z-axis is shown for the event shown in Fig. 14(a) using 73 individually resolved Cherenkov photons. (For interpretation of the references to color in this figure caption, the reader is referred to the web version of this paper.)

coverage. The slope of the linear fit, multiplied by the weighted average of the group velocity ($\langle v_{group} \rangle$), is the tangent of the track angle.

It is possible to separate the direct and mirror-reflected photons when using the position-corrected time, t' , as shown in Fig. 17. A normal view time-cut of < 1.95 ns and a stereo view time-cut of < 1.90 ns were used on the data to isolate the direct photons. The number of direct Cherenkov photons per event is shown in Fig. 20(a). The sample fitted consists of 522 events with more than 8 normal-view and more than 4 stereo-view direct photons are fit, requiring that each PM has at least two direct photons. Separate linear fits to the direct stereo and normal view photons are performed. The fits are reasonable, as shown by the distributions of χ^2 per degree of freedom in Fig. 20(b).

The returned slopes from the fits, $\frac{dt'}{dz}$, are multiplied by $\langle v_{group} \rangle = (c/1.38)$ and histogrammed in Fig. 21. Linear fits to the photons in the direct normal-view yield an angle relative to the nominal beam axis over all the fitted tracks of 73 ± 60 mrad at 1σ resolution. The stereo view shows a measurement of -20 ± 121 mrad. The stereo view measurement has a larger error that is most likely due to its smaller z -coverage than the normal view, which gives it a smaller lever arm on the angular measurement. The normal view

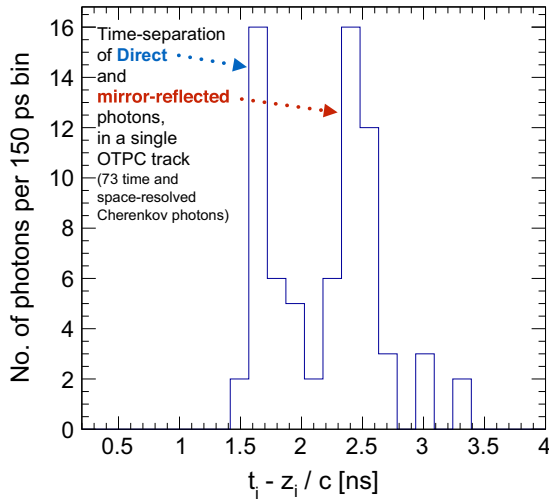


Fig. 19. Histogram of the detected photon times from the event in Fig. 18, plotted using the position-corrected time introduced in Fig. 17. The separated peaks in the time distribution are from the direct and mirror-reflected Cherenkov photons.

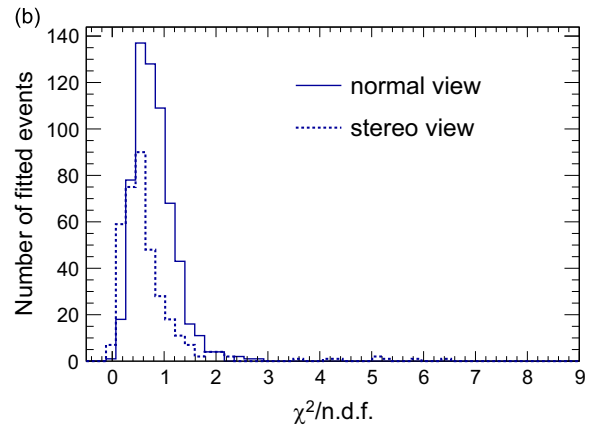
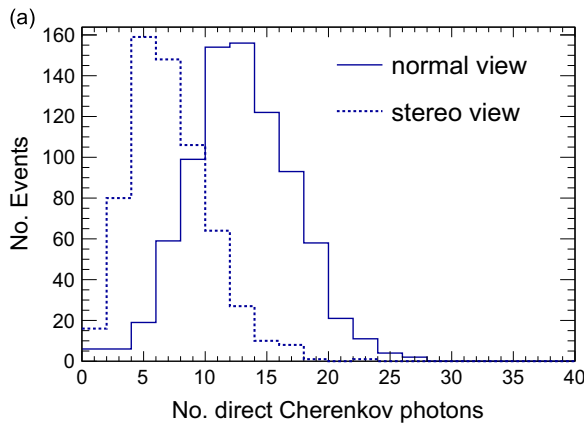


Fig. 20. (a) Number of direct Cherenkov photons per event. The direct and mirror-reflected photons are separated by applying a time-cut to the data presented in Fig. 17. (b) Goodness of fit as given by the χ^2 per number of degrees of freedom (n.d.f.). Events from (a) with more than 8 normal-view and more than 4 stereo-view direct photons are used in the fit.

has 3 equally spaced PMs over a z -range of ~ 40 cm, but the stereo view has 2 PMs covering a z -range of only 20 cm.

12. Spatial resolution

To fully reconstruct charged particle tracks, the mirror-reflected photons are used in combination with the direct Cherenkov light. A second time cut is made on the position-corrected time, t' (Fig. 17), to isolate the reflected Cherenkov photons. A normal view time-cut of > 2.05 ns and a stereo view time-cut of 2.0 ns were used on the data. A time-gap of 100 ps between the direct and reflected photon time-cuts was used to separate the two regions.

The number of reflected photons per event in the normal and stereo views is shown in Fig. 22(a). The relative number of direct and reflected detected photons at each PM per event per cm is shown in Fig. 22(b). As expected from Fig. 17, there is a preponderance of reflected over direct photons.

A straightforward way to reconstruct the spatial position of the trajectory is to take the difference of the mean direct photon arrival times and the mean reflected photon arrival times in the t' basis. Explicitly, the time difference at a PM for a given event a ,

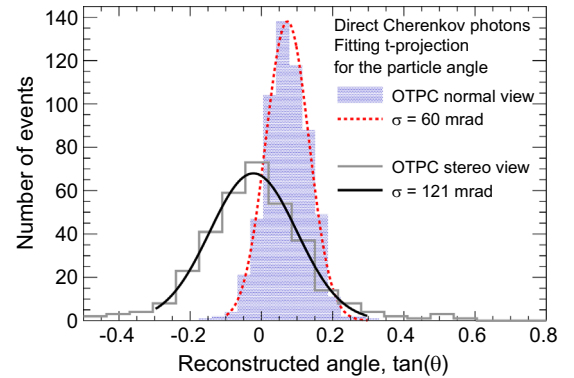


Fig. 21. Measured angle of tracks along the z -axis as seen by the stereo and normal views. The direct Cherenkov light is fit with a straight line for events with more than 8 direct normal-view photons. In the stereo view, at least 4 photons are required to fit the angle. The measured angle distributions are 73 ± 60 mrad for the normal view and -20 ± 121 mrad in the stereo view. Fits that have a $\chi^2/n.d.f.$ greater than 3, as shown in Fig. 20(b), were not included in this measurement.

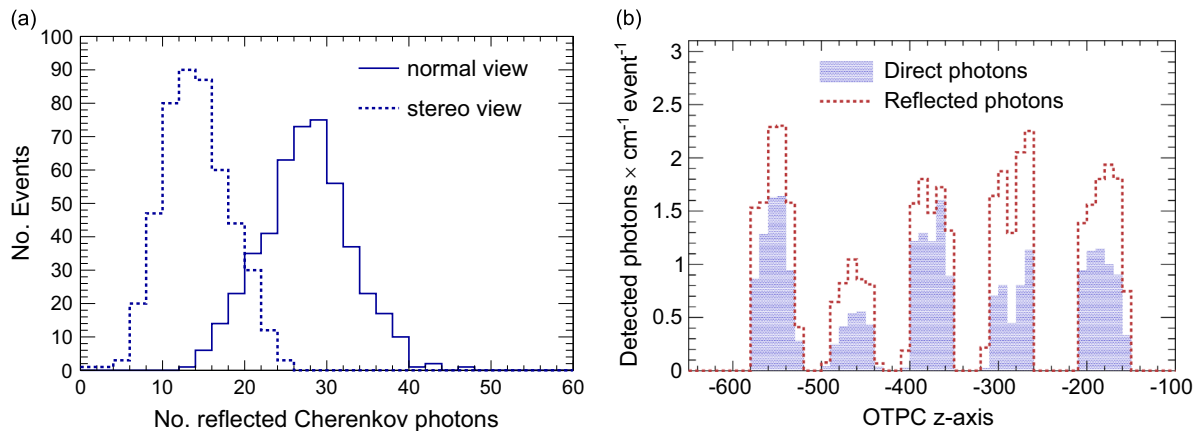


Fig. 22. (a) Number of reflected Cherenkov photons per event. The direct and mirror-reflected photons are separated by applying a time-cut to the data presented in Fig. 17. The number of direct photons per event is shown in Fig. 20(a). (b) Number of direct and reflected photons detected per event per cm. The five discrete distributions along the OTPC z-axis are the 5 PM locations (left to right, PMs 0–4).

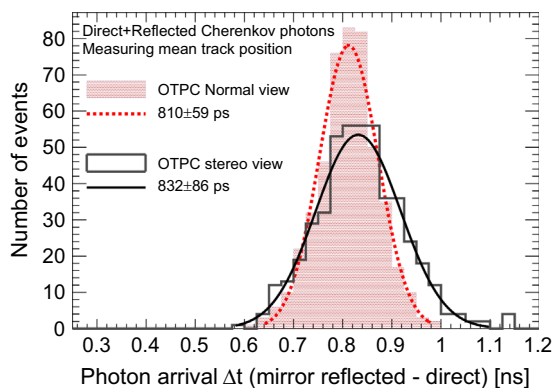


Fig. 23. Time-of-arrival difference between the direct and mirror reflected Cherenkov photons for the normal and stereo views. The time differences were measured using Eq. (9). The normal view has an average time difference of 810 ± 59 ps and the stereo data shows a time difference of 832 ± 86 ps.

Δt_{PM} , using this method is

$$\Delta t_{PM} = \frac{1}{n} \sum_{i=1}^n t_i^{mirror} - \frac{1}{m} \sum_{j=1}^m t_j^{direct} - t_{ref} \quad (9)$$

where n is the number of reflected photons per event per PM and m is the number of direct photons per event per PM. A time reference for the event, t_{ref} (the R_2 trigger signal time), is subtracted from each event for alignment. This time-difference measurement is inserted into Eq. (6) to obtain the lateral displacement of the particle track.

The result of Eq. (9) is shown in Fig. 23 when grouping together the normal view data and stereo view data separately. This result incorporates the same 522 events used in the measurement shown in Fig. 21. The normal view has an average time difference of 810 ± 59 ps; the stereo data show a time difference of 832 ± 86 ps.² These 1σ uncertainties correspond to spatial resolutions of 9.6 mm and 13.9 mm, respectively, when combining data from the PMs.

To utilize the OTPC as a tracking detector, we use each PM to resolve the spatial coordinates along the z- and ϕ -axes. We require that an event has more than three direct and three mirror-reflected photons for each PM. There are 127 through-going

events that satisfy this condition. As expressed in Eq. (9), the radial position, r , along the z and ϕ axes of the OTPC is defined as the displacement from the nominal beam axis. Using Eqs. (9) and (6) we can reconstruct r at each of the five PM positions in z- and ϕ . The five distributions in the radial position are shown in Fig. 24.

The properties of the data in Fig. 24 are shown in Table 1. The reconstructed radial position, r , at each z position is consistent with $r=0$, which is the expectation with the through-going trigger. At each normal view PM, the resolution is about 15 mm on this measurement. On the stereo view, the average error is 17.5 mm. We expect the beam spatial location to have an RMS variation of ~ 7 mm from the measured beam output position in the R_2 trigger.

Fig. 25 shows the 3D track reconstruction of the event displayed in Fig. 14(a) and Fig. 18. The direct Cherenkov photons are projected onto the reconstructed radial position, r , and the OTPC normal and stereo-view coordinates are decomposed into the Cartesian coordinate system defined in Fig. 2.

13. Conclusions

We have constructed and characterized the performance of a small prototype optical-TPC (OTPC), in which we measured the time and position of arrival for each individual photon emitted by Cherenkov radiation from a charged particle traversing the water volume. The photon arrival times and 2D spatial locations are resolved to ~ 75 ps and $\leq 3 \times 3$ mm², respectively, using the digitized waveforms. Given the arrival positions and the drift times, the particle track position and direction can be reconstructed.

The ability of the OTPC to resolve time differences much smaller than 1 ns lends itself to two strategies relevant to the economics of scale-up for larger detectors. The first was to cheaply multiply the $\sim 7\%$ photocathode coverage on the surface of the detector by using optical mirrors; the mirrors more than doubled the OTPC light collection in our setup. For each track, the mirrors allowed for the added collection of Cherenkov photons impinging on the detector wall opposing the MCP-PMT. The reflected photons are clearly time-resolved in the data with an average delay of 770 ps compared to the direct Cherenkov light. The second strategy is to digitize the microstrips at one end of the strip with the opposing end open, so that direct pulse and the reflection from the far end provides two distinct \sim ns-wide pulses per detected photon. This cuts the electronics channel count in half, and has the added advantage that the times-of-arrival at each end are measured on the same electronics channel.

² The mean time differences are slightly larger than measured on the full 16 GeV/c dataset (Section 10.1 and Fig. 17) due to the event selection and the time cuts applied to separate the direct and mirror-reflected photons described in the text.

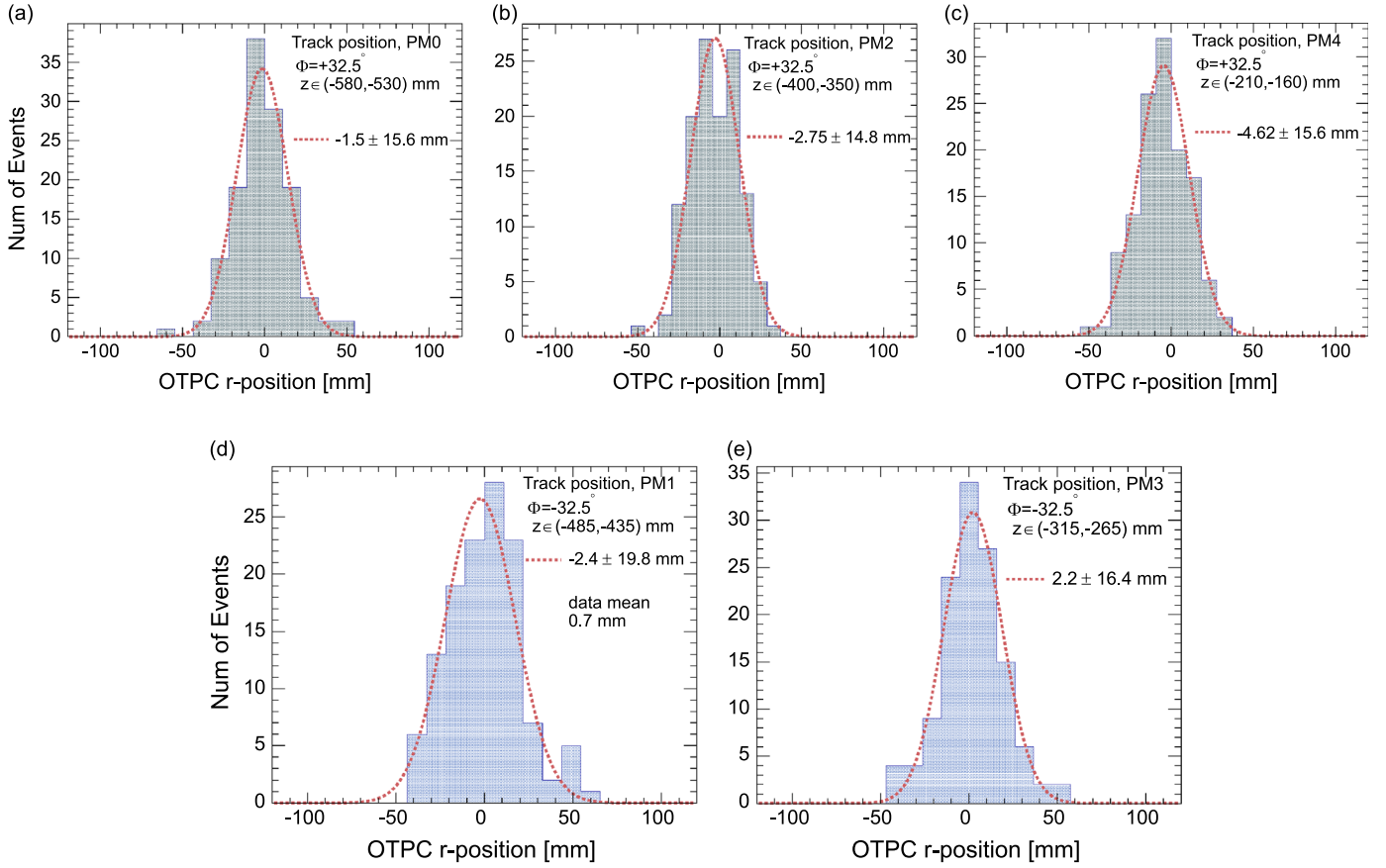


Fig. 24. The reconstructed radial track position along the OTPC z-axis at each PM ϕ -location.

Table 1

Average reconstructed radial positions of tracks along OTPC z-axis. The OTPC center-line is defined as $r=0$. These data are shown in Fig. 24.

PM	\bar{z} (mm)	ϕ (radians)	Reconstructed r (mm)
0	-550	0.567	-1.5 ± 15.6
2	-375	0.567	-2.75 ± 14.8
4	-185	0.567	-4.62 ± 15.6
1	-460	-0.567	0.7 ± 19.8
3	-290	-0.567	2.2 ± 16.4

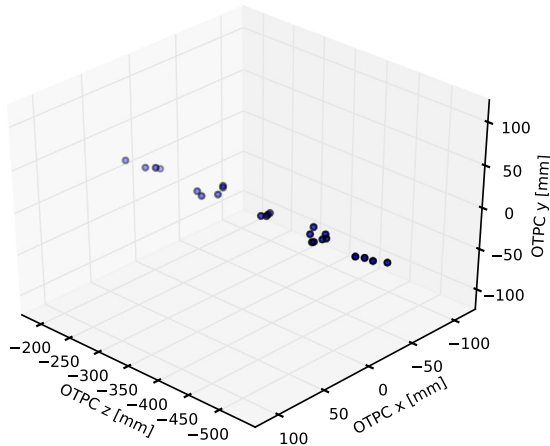


Fig. 25. The 3D track reconstruction of the event shown in Fig. 14(a) and Fig. 18. The position-corrected times, t'_i , of the direct Cherenkov photons are projected on the reconstructed radial position (stereo, normal, z) and decomposed into Cartesian (x,y,z) coordinates.

For through-going tracks recorded at a secondary beam momentum of 16 GeV/c, we observed 80 ± 20 detected Cherenkov photons per event. Each photon is resolved in time, z , and ϕ , allowing a view of the 3D trajectory. We measured an angular resolution, assuming a straight track, of 60 mrad when fitting events in which more than 8 direct photons were detected among the three MCP-PMTs in the OTPC normal view. By time-resolving the direct and mirror reflected photons at 59 ps, we measure a transverse resolution on the average particle track of ~ 10 mm. When measuring the photon time-difference at the level of the individual PMs, we measure a track resolution of about 15 mm along the OTPC z-axis. We note that an entire reconstructed event takes place over a 40-cm track length and in a duration of less than 3000 ps.

Acknowledgments

We thank the staff of the Enrico Fermi Institute Electronics Development Group for their essential technical and intellectual contributions, in particular Mircea Bogdan for the design of the Central DAQ printed-circuit card, Mark Zaskowski for electronics assembly, and Mary Heintz for her superb support of the infrastructure for electronics design, computing, and web documentation. We are indebted to Richard Northrop and Robert Metz, both of the University of Chicago Physical Sciences Division Engineering Center, for expertise in mechanical design and skilled machining, respectively.

We express our gratitude to Jeffrey DeFazio, Raquel Ortega, and Emile Schyns of PHOTONIS, Inc., for providing technical details and support for the Planacon photodetectors. We thank Howard Nicholson, then of the DOE, for suggesting the use of LAPPDs for

neutrino physics and for the name of the Optical Time Projection Chamber.

This work could not have been done without the support of Fermilab and, in particular, the Fermilab Test Beam operations group: Eugene Schmidt Jr., Erik Ramberg, Mandy Rominsky, and Aria Soha. Todd Nebel and Greg Sellberg provided excellent mechanical support. The LArIAT collaboration provided technical assistance and knowledge in welcoming the OTPC operation parasitically in their beam line.

This work was supported by National Science Foundation Grant PHY-1066014 and Department of Energy Award DE-SC0008172. Part of this work was performed at the Fermilab Test Beam Facility, which is operated by Fermi Research Alliance, LLC under Contract no. De-AC02-07CH11359 with the United States Department of Energy.

References

- [1] P.A. Čerenkov, *Physical Review* 52 (August) (1937) 378.
- [2] J. Beringer, et al., *Physical Review D* 86 (2012) 323.
- [3] B.W. Adams, A. Elagin, H.J. Frisch, R. Obaid, E. Oberla, A. Vostroikov, R. G. Wagner, J. Wang, M. Wetstein, *Nuclear Instruments and Methods in Physics Research Section A* 795 (2015) 1.
- [4] J. Milnes, J. Howarth, *SPIE USE* 8 (2004) 89.
- [5] O.H.W. Siegmund, A.S. Tremsin, J.V. Vallerga, R. Abiad, J. Hull, *Nuclear Instruments and Methods in Physics Research Section A* 504 (2003) 177.
- [6] N. Kishimoto, M. Nagamine, K. Inami, Y. Enari, T. Ohshima, *Nuclear Instruments and Methods in Physics Research Section A* 564 (2006) 204.
- [7] F. Tang, et al. Transmission-line readout with good time and space resolutions for Planacon MCP-PMTs, In: *Topical Workshop on Electronics for Particle Physics*, CERN 2008, 2008, pp. 579–583.
- [8] H. Grabas, H.J. Frisch, E. Oberla, J.-F. Genat, R. Northrop, D. McGinnis, B. Adams, M. Wetstein, R. Obaid, F. Tang, *Nuclear Instruments and Methods in Physics Research Section A* 711 (2013) 123.
- [9] B.W. Adams, A. Elagin, H.J. Frisch, R. Obaid, E. Oberla, A. Vostroikov, R. G. Wagner, M. Wetstein, *Nuclear Instruments and Methods in Physics Research Section A* 732 (2013) 392.
- [10] E. Oberla, H. Grabas, J.-F. Genat, H.J. Frisch, K. Nishimura, G. Varner, *Nuclear Instruments and Methods in Physics Research Section A* 735 (2014) 452.
- [11] J. Ahrens, et al., *AMANDA*, *Nuclear Instruments and Methods in Physics Research Section A* 524 (2004) 169.
- [12] I. Anghel, E. Catano-Mur, M.C. Sanchez, M. Wetstein, T. Xin, Using Fast Photosensors in Water Cherenkov Neutrino Detectors, DPF 2013, [arXiv:1310.2654](https://arxiv.org/abs/1310.2654), 2013.
- [13] ANNIE Collaboration, Letter of Intent: The Accelerator Neutrino Neutron Interaction Experiment (ANNIE), [arXiv:1504.0180](https://arxiv.org/abs/1504.0180), 2015.
- [14] C. Aberle, A. Elagin, H.J. Frisch, M. Wetstein, L. Winslow, *Journal of Instrumentation* 9 (06) (2014) P06012.
- [15] LAPPD Collaboration Website (<http://www.psec.uchicago.edu>).
- [16] M.J. Minot, et al., *Nuclear Instruments and Methods in Physics Research Section A* 787 (2015) 78.
- [17] B.W. Adams, M. Chollet, A. Elagin, R. Obaid, E. Oberla, A. Vostroikov, M. Wetstein, P. Webster, *Review of Scientific Instruments* 84 (2013).
- [18] PHOTONIS USA Pennsylvania, Inc, Planacon XP85022 32 × 32 Datasheet (<http://www.photonisusa.com>), January 2014.
- [19] Optical data from: (1) Enhanced Aluminum 4–6 λ First-Surface Mirror, Edmunds Optics, (2) Fused-silica glass port, and (3) Optical coupling gel, code 0607, Cargille Labs. Spray paint used for light absorbing surfaces: Rust-oleum, textured, indoor/outdoor, black (<http://www.mcmaster.com>).
- [20] S. Seibert, A. LaTorre, Fast Optical Monte Carlo Simulation With Surface-Based Geometries Using Chroma (<http://www.chroma.bitbucket.org/>), 2011.
- [21] J.D. Jackson, *Classical Electrodynamics*, 3rd ed., John Wiley & Sons, Inc., New York, NY, 1999.
- [22] I. Tamm, I. Frank, *Comptes Rendus de l'Academie des Sciences de l'URSS* 14 (1937) 109.
- [23] M. Daimon, A. Masumura, *Applied Optics* 46 (2007) 3811.
- [24] Samtec, Inc. 34 AWG Micro Coax Cable Datasheet, May 2015.
- [25] K. Nishimura, A. Romero-Wolf, *Physics Procedia* 37 (2012) 1707.
- [26] D. Stricker-Shaver, S. Ritt, B.J. Pichler, *IEEE Transactions on Nuclear Science NS-61* (December (6)) (2014) 3607.
- [27] Fermilab Test-Beam Facility (<http://ppd.fnal.gov/ftbf/>).
- [28] F. Cavanna, et al., LArIAT: Liquid Argon In A Testbeam, [arXiv:1406.5560](https://arxiv.org/abs/1406.5560), 2014.
- [29] T.J. Roberts, D.M. Kaplan, G4beamline simulation program for matter-dominated beamlines, In: *Particle Accelerator Conference, 2007 PAC*, Albuquerque, NM, IEEE, 2007, pp. 3468–3470.
- [30] E. Oberla, Charged particle tracking in a water Cherenkov optical time-projection chamber (Ph.D. thesis), University of Chicago, July 2015.
- [31] Advanced Laser Diode Systems, Picosecond Diode Laser – PiLas Manual and Test Report, June 2013.